Soft Matter

Determination of mosaicity in oriented stacks of lipid bilayers

John F. Nagle,* Kiyotaka Akabori, Bradley W. Treece and Stephanie Tristram-Nagle

Two methods of measuring the misorientation of domains in oriented multilamellar stacks of lipid bilayers superficially appeared to give different values for the mosaic spread. It is first shown that the traditional rocking method and a newer ring method give the same value of the mosaic spread when the two types of data are similarly analyzed. Both indicate a long-tailed, nearly Lorentzian, mosaic distribution function. Our primary innovation is the analysis of ring data as a function of the rocking angle. For our best oriented DOPC sample, this analysis is consistent with a single Lorentzian mosaic distribution function with width 0.05°. In contrast, samples of DMPC indicate a more complex mosaic distribution and larger widths.

1. Introduction

In X-ray studies of model systems of biomembranes consisting of lipid bilayers, often with additives such as peptides,[1–5] strong scattering intensity is provided by smectic liquid crystalline multilamellar arrays. Globally isotropic multilamellar vesicles are easily prepared.[6–9] While more difficult to prepare, oriented stacks of bilayers provide two-dimensional information that enables the determination, by low angle X-ray scattering (LAXS), of the fundamental bending modulus that pertains to the flexibility of membranes and they enable better determination of structure *via* the transbilayer electron density profile by providing data to larger q values.[10] In the most biologically relevant fluid phase case, the bilayers in the stacks consist of in-plane isotropic sheets, so the LAXS diffraction pattern consists only of peaks along the meridian in the q_z direction, where z is normal to the substrate. However, even with the best preparation, oriented stacks are subject to the artifact of mosaic spread. Within the sample size illuminated by an X-ray beam there are many domains consisting of well correlated stacks of bilayers whose bilayer normals are oriented at relative angle α to the substrate normal which is also the mean normal of the many domains. As the bilayers in each domain are in-plane powders and there is only one-dimensional stacking order, the only characterizing parameter for the mosaicity is the angle α between the normal to a domain and the normal to the substrate; this is simpler than the more complex pole figure characterization of general thin films consisting of crystallites.[11–13]

Typical illuminated volumes in our experiments are 0.3 mm wide, corresponding to the beam width, 5 mm along the beam direction, and 10 μm thick (~1600 bilayers) in the direction

Department of Physics, Carnegie Mellon University, Pittsburgh, Pennsylvania 15213, USA. E-mail: nagle@cmu.edu

perpendicular to a substrate supporting the stack. Well correlated scattering domains have much smaller sizes estimated to be of order 0.1 μm,[14] so there are many domains present and it is appropriate to consider continuous angular mosaic distributions $g_M(\alpha)$ and to report w, the full width at half maximum (FWHM), as the mosaic spread. It should be noted that, while these domains are macroscopically small, they are microscopically large enough to study the fundamental properties of bilayers.

Although mosaicity can be quite small,[15–17] it is important in the analysis of scattering data to ascertain that it is either negligible or to make corrections for samples that have large mosaic spread w. We have made such corrections for the analysis of low angle X-ray scattering (LAXS) that gives the bending modulus K_C, the compression modulus B, and the form factor $F(q_z)$ that gives structure along the normal to bilayers.[10] We have also made corrections for the analysis of wide angle X-ray scattering (WAXS) from which an X-ray order parameter can be obtained.[18]

A concern that has arisen is that two different ways of viewing and measuring mosaicity have seemed to indicate different values for the mosaic spread w. Traditional rocking scans of oriented lipid bilayers often indicate negligibly small values of w.[15] In contrast, as seen in Fig. 1, the azimuthal intensity of the rings that emanate from sharp peaks and also the clear appearance of many orders[19] suggest, at least superficially, that w is larger by an order of magnitude than obtained from the rocking scans. In this paper we first confirm that the appropriate analysis of the ring data gives the same small value of w as rocking data, as it should, since ring data are really just rocking scans in the orthogonal direction. The apparently large mosaicity suggested by Fig. 1 is due partly to long, nearly Lorentzian, tails emanating from the very intense central peak that is partly attenuated by an absorber
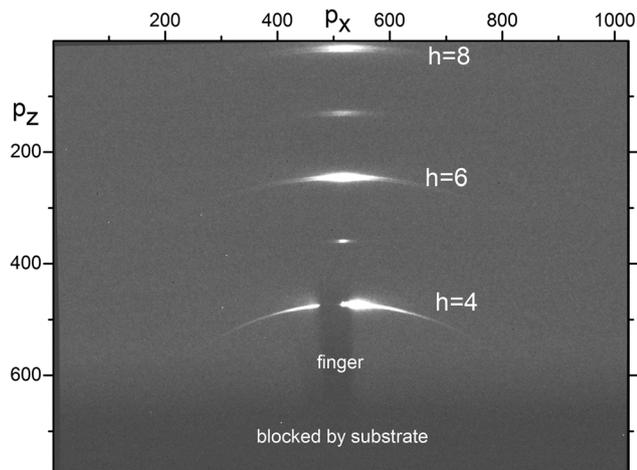
Fig. 1 CCD grayscale intensity *versus* pixel numbers (p_x,p_z) for a 120 s exposure of dry DMPC at a fixed angle $\omega = 2.6°$. The Bragg angle of the $h = 4$ peak and its central ring were attenuated by a deliberately slightly off center 1 mm wide 100 μm finger of Mo that does not extend as high as the scattering from the $h = 5$ peak. The $h = 5–8$ peaks are visible with prominent circular arcs emanating from $h = 6$ and 8. Orders $h = 1$ and 2 were blocked by the substrate and $h = 3$ was attenuated by the finger. Background intensity was about 70 compared to 10 000 in the most intense unattenuated portion of the $h = 4$ ring. Much shorter exposures showed that the intensity of the peak would be 1.2×10^7, far exceeding the dynamic range (64×10^3) of the CCD detector.

in that figure. Indeed, the amount of misoriented sample that scatters into those tails is quite small compared to the total sample. Perhaps most importantly, we also perform an analysis of ring data on rocking scans that provides evidence that many samples have a more complex mosaic distribution that is not transparent from rocking scans; that also partly accounts for the appearance of many orders in fixed angle exposures.

After describing experimental techniques in Section 2, Section 3 presents the data for a dry sample for which analysis gives the same mosaic width from ring data as from rocking data. Section 4 extends Section 3 by considering ring data from the rocking scans and it presents a toy model that provides insight into the results. Section 5 presents the same kind of data as in Section 4 for other lipids, including for well hydrated samples. Section 6 mentions additional considerations that affect the analysis of mosaic spread, followed by discussion and summary in Section 7.

2. Experimental

2.1 Sample preparation and X-ray setup

The rock and roll technique[20,21] was used to prepare samples of mean thickness 10 μm on Si wafers, 15 mm along the beam direction by 30 mm in the transverse direction. The lipid was then trimmed from 15 mm to a central 5 mm strip. Samples were placed in a chamber remaining open to air with relative humidity ∼30% for "dry" samples. For "wet" samples, the chamber, containing a reservoir of water, was closed and the samples were hydrated from water vapour to essentially

100% RH as seen by the lamellar repeat D spacing increasing nearly to that of fully hydrated multilamellar vesicles dispersed in liquid water.

X-rays at the Cornell High Energy Synchrotron Source (CHESS) were monochromated by W/B$_4$C multilayers to $\lambda = 1.175$ Å and 1.3% dispersion. For a few data with 100 times better energy resolution a channel cut Si crystal was added between the multilayer monochromator and the sample. The FWHM of the beam in the horizontal direction was 0.3 mm for high energy resolution and 0.2 mm for low energy resolution. Most data were collected on a CCD (Finger Lakes Instrumentation, Lima, NY) with 1024 × 1024 pixels, each of average size 0.07113 mm. Distortion and intensity corrections, dark background, and dezingering were performed by standard CHESS software.[22] A rotation motor (Airlines Manufacturing, Bensalem, PA) built into the sample chamber enabled changes in ω, the angle between the beam and the substrate; 0.05 degrees was the smallest semi-reproducible angular increment. Some data were also collected with an in-house rotating anode (Rigaku model RUH3R, $\lambda = 1.54$ Å and a Rigaku Mercury CCD detector) with the same sample chamber and rotation motor. High angular resolution (0.0005 degrees) rocking scans on a dry sample were also obtained with a fixed tube source with a Ge analyzer crystal (PANalytical X'Pert MRD Pro).

2.2 Rocking data $I_R(\omega)$

Short exposures at CHESS, typically 1 or 3 seconds, were usually taken in a sequence of increasing angles ω between the substrate and the beam with an example shown in Fig. 2. For each ω there is a small peak at 2ω which is the specular reflection of the beam, primarily from the Si substrate; the intensity of these specular peaks decreases with increasing ω because ω is greater than the
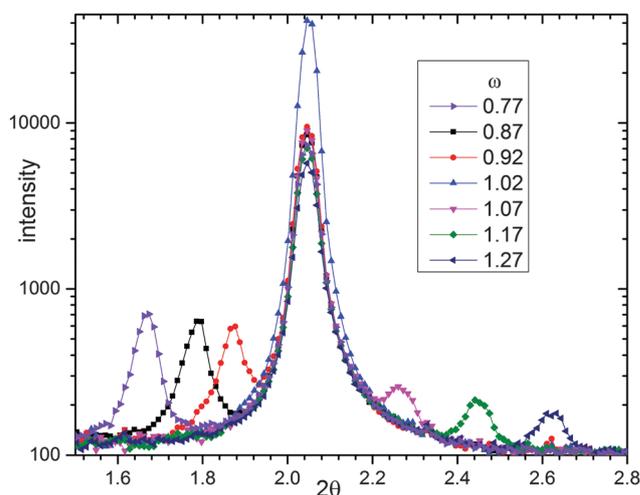

Fig. 2 Log of intensity for several fixed substrate angles ω as a function of angle 2θ along the meridian. As ω was increased, the position of the specular peak increased and its intensity decreased. The position of the $h = 2$ scattering peak remained at the same value of $2\theta = 2.06°$ corresponding to its Bragg angle $2\theta_B$ (with a small offset). The intensity of the $h = 2$ peak when $\omega = 1.02°$ became considerably larger, by more than 60 times the interpolated specular intensity. The sample was hydrated DOPC at 30 °C.

critical angle for total reflectivity for Si. The large peak in Fig. 2 is the diffraction peak that occurs at $2\theta_B$, where θ_B is the Bragg angle for the selected order. As expected, its intensity increases as ω approaches the Bragg angle θ_B. For small $\omega - \theta_B$ the CCD became overexposed, so one or more attenuators of nominally 25 μm thick molybdenum were inserted into the beam, each attenuator calculated to decrease the beam intensity by a factor known to be 6.2 for the nominal thickness (http://www.cxro.lbl.gov) at $\lambda = 1.175$ Å, but that we calibrated to be 7.0, corresponding to attenuator thickness of 26.7 μm for pure Mo. The rocking intensity $I_R(\omega)$ was obtained by summing the intensity in a box of 4×4 CCD pixels centered on the peak intensity at twice θ_B, the Bragg angle.

2.2 Ring data $I_r(\eta)$

Exposures at a fixed angle ω exhibited a peak at $2\theta_B$ on the meridian of the CCD accompanied by circular rings. These rings were quantified by the intensity $I_r(\eta)$ where the ring angle η is zero for the center of the ring on the meridian where the intensity was greatest. $I_r(\eta)$ data for small η were obtained from the short CCD exposures obtained for the rocking scans. For our best sample, $I_r(\eta)$ for large η was obtained from longer exposures with a 100 μm Mo finger downstream from the sample that attenuated the central peak scattering by 2400, as shown in Fig. 1. By systematically moving the finger to attenuate more of the central peak, longer exposures up to 120 s were taken to obtain good statistics in the various $\Delta\eta$ sectors of the unattenuated tails of the ring; overlap of the exposed sectors for the different finger positions enabled determination of the smallest η at which the intensity was not partially cut off by the attenuator. Piecing these different exposures with the finger together with those with no finger yielded $I_r(\eta)$ for η up to ~25 degrees. For dry samples, the background intensity was constant and was subtracted. For well hydrated samples, diffuse scattering intensity acts as a non-constant background which was subtracted by averaging the intensity in two concentric rings, one with radius slightly larger than the mosaic ring, and one smaller. The intensities of the central ring and the background rings were each averaged over 3 pixels in the radial direction at intervals of 0.05° in η. The range of ring intensities spanned three orders of magnitude; estimated errors used for fitting were empirically determined to be 0.2 $I^{1/2}$ by examining noise levels in different intensity ranges.

Non-linear least squares fitting of Lorentzians, Gaussians, and Voigtians (the convolution of a Lorentzian and a Gaussian) were performed using Origin 9.1 (OriginLabs, Northampton, MA, USA).

3. Results for dry samples

3.1 Rocking results

Fig. 3a shows rocking data $I_R(\omega)$ for the dry DMPC sample in Fig. 1; it had a lamellar repeat spacing $D = 51.8$ Å corresponding to a Bragg angle $\theta_B = 2.6°$ for the $h = 4$th order. The data were taken in two successive rocking scans with some additional
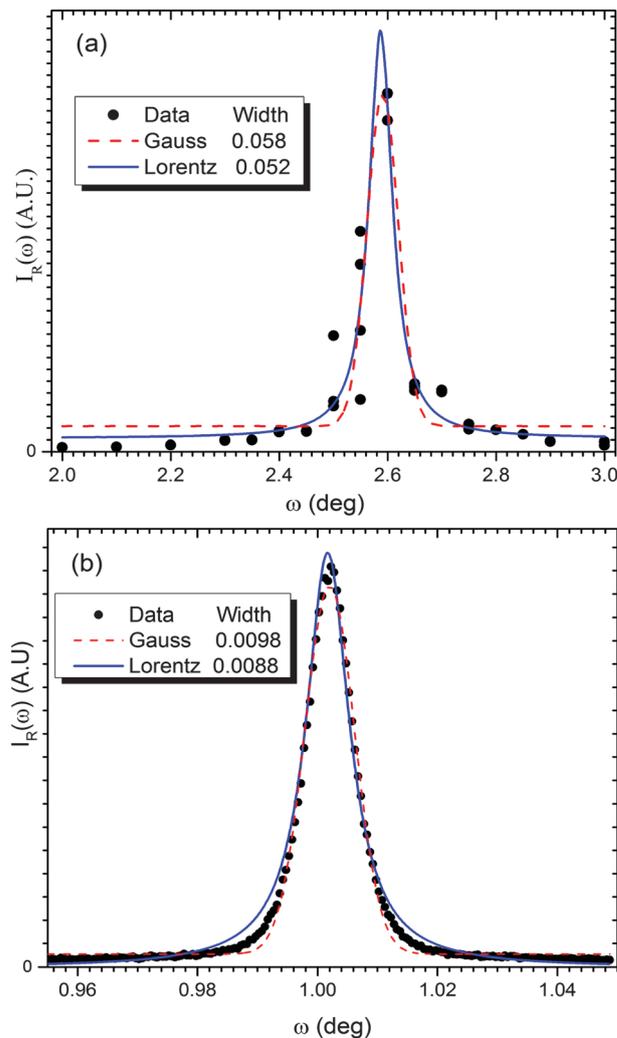

Fig. 3 Intensities $I_R(\omega)$ near Bragg angle θ_B (a) for the $h = 4$ peak of dry DMPC using our primary setup at CHESS and (b) for the $h = 1$ order of dry DOPC using high angular resolution.

exposures near the peak angle. The intensity at $\theta = 2.55°$ was especially irreproducible which we attribute to our rotation motor occasionally not advancing by 0.05° and then advancing 0.1° at the next step. Notwithstanding this experimental artifact, there was a clear increase in intensity of two orders of magnitude within a narrow angular range. The Gaussian and Lorentzian fits to the data in Fig. 3 show that the Lorentzian fits much better in the tails. Note that the scattered intensity would decrease as ω approaches 0 due to increased absorption of the incident beam by the sample and also as ω approaches $2\theta_B$ due to increased absorption of the scattering by the sample. While correcting for this would tend to flatten the intensity in the tails, improving the Gaussian fit, calculation using the absorptivity of lipid at the used wavelength and thickness of the sample shows that the absorption correction is negligible over the measured angular range, supporting the conclusion that the mosaic distribution is not Gaussian. The fitted Lorentzian width of this sample was $w = 0.052 \pm 0.012°$, comparable to literature results.[15–17]

Much higher angular resolution data are shown for dry DOPC in Fig. 3b. To compensate for the weaker fixed tube X-ray source, the very intense $h = 1$ peak was studied. Although neither the Lorentzian or the Gaussian fit is perfect, either indicates a very narrow width less than $0.01°$.

3.2. Ring results

Fig. 4 shows the intensity $I_r(\eta)$ around the $h = 4$ ring when $\omega = \theta_B$. The data in the tail for the largest positive η range were obtained from Fig. 1. Data for small $|\eta|$ were obtained with 1 s exposures and a 25 μm Mo attenuator in the beam upstream from the sample and no downstream attenuation of the central $h = 4$ peak. The beam intensity with no sample has a FWHM w_B that corresponds to $0.46°$ in η in the $h = 4$ ring at our sample to detector distance, so the mosaic distribution w is not instrumentally resolvable just from the central peak in Fig. 4. The inset to Fig. 4 shows that there is a long η tail in the ring intensity. (It is important to note that the intensity for the largest η does not come from a long tail of the beam. While the beam is fairly well fit by a Gaussian, it also has an excess long tail intensity in the horizontal direction, which, however, decays more rapidly than the sample data. Furthermore, the intensity from a sample with zero mosaicity that would ensue from a beam tail would occur along a horizontal trajectory on the CCD detector, whereas the maximum intensity follows a ring trajectory on the CCD. Nevertheless, these two trajectories are asymptotically identical for small η, so it is difficult to separate the two effects when only data for small η are available.).

The straight solid magenta line in the log–log plot in the inset to Fig. 4 indicates that the tail of $I_r(\eta)$ can be described as an $\eta^{-2.7}$ power law. Also shown in both the inset and the main Fig. 4 is the fit to a Gaussian. While the Gaussian provides a good fit to the
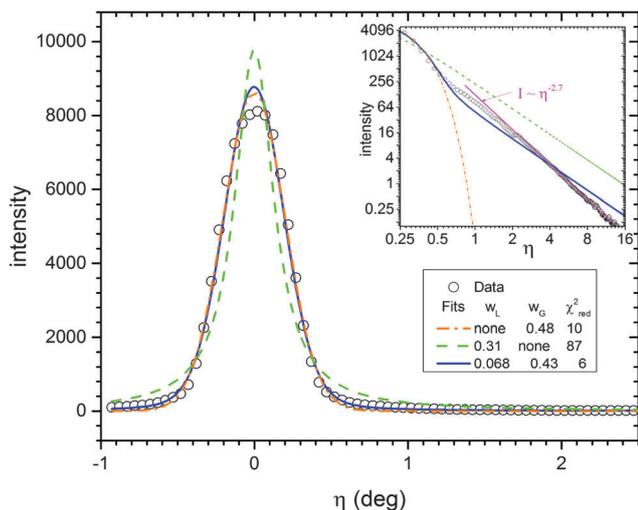

Fig. 4 Intensity $I_r(\eta)$ versus the azimuthal angle η from the meridian (perpendicular to the oriented stack) taken with incident angle $\omega = 2.6° = \theta_B$ from the DMPC rocking data in Fig. 3a. The solid blue line shows a Voigtian fit with a Lorentzian FWHM $= 0.068 \pm 0.001°$ and a Gaussian FWHM $= 0.43 \pm 0.01°$. The dashed green line shows a Lorentzian fit and the dot-dashed orange line shows a Gaussian fit.

central peak, it clearly decays much too rapidly in the tails as emphasized in the inset. The slower η^{-2} decay of a Lorentzian fit represents the tails better than a Gaussian but it is a poor fit to the central peak causing it to have the largest reduced χ^2 as displayed in the legend to Fig. 4 which also shows the FWHM of the fits. Our best global fit is to a Voigtian, which is the convolution of a Lorentzian, which nearly describes the mosaic distribution, with a Gaussian, which nearly describes the beam. The Voigtian fits both the central peak and the tails rather well, considering the different power law exponents. As shown in the legend, the Voigtian fit gives a FWHM w_L for the Lorentzian part that agrees quite well with the Lorentzian width obtained from the rocking data in Fig. 3. We propose henceforth to fit ring data with a Voigtian, primarily assigning or even constraining w_G to the beam width and assigning the ensuing w_L as the mosaic width, noting that this value of w_L overestimates the mosaic width when the beam also has tails longer than Gaussian.

One major consequence of a power law decay is that it makes it partly understandable why many off-specular orders are observable when ω is fixed. If the distribution were Gaussian with a width of $0.068°$, the $h = 8$ peak would be reduced by 10^{-300}, clearly unobservable. With a Lorentzian, the reduction is about 10^{-3}, considerable but still observable, if only barely. The next section will add another reason that the off-Bragg reflections are observed.

4. Ring widths of non-Bragg rings

We have gained a valuable perspective for mosaicity by examining the ring widths w_L of the same fixed angle exposures that were used to obtain the rocking data, namely for all values of $\omega - \theta_B$, not just when $\omega = \theta_B$. Fig. 5 shows normalized $I_r(\eta)$ data for several values of the fixed angle ω for the same DMPC sample as in Fig. 1, 3 and 4. It is apparent that the widths of the ring increase as $|\omega - \theta_B|$ increases. Voigtian fits with the Gaussian width fixed to $0.43°$ yield the Lorentzian widths w_L shown in the inset to Fig. 5.

If the mosaicity were Gaussian, it is easy to show that the ring width would be the same for all ω. In contrast, if the mosaic distribution were Lorentzian with mosaic width w_M, then

$$I_r(\eta,\omega,w_M) = w_M/[w_M^2 + 4(\eta^2 + (\omega - \theta_B)^2)], \qquad (1)$$

for which the FWHM $w_L(\omega)$ of the ring with fixed ω is given by

$$w_L = \sqrt{w_M^2 + 4(\omega - \theta_B)^2}. \qquad (2)$$

This is plotted in the inset to Fig. 5 with $w_M = 0.06°$, the average of the rocking result in Fig. 3 and the extensive ring result for $\omega = \theta_B$ in Fig. 4. It is apparent, again, that a Lorentzian represents the data better than a Gaussian. However, eqn (2), while consistent with an increase in w_L with increasing $|\omega - \theta_B|$, clearly deviates substantially from the data, even when fits are made to all the data, as shown by two dot-dashed curves in the inset to Fig. 5.

To obtain insight into this disagreement, we consider a toy example. Suppose that a sample consists of a well oriented fraction f_1 with Lorentzian mosaicity assigned as $w_{M1} = 0.1°$ and
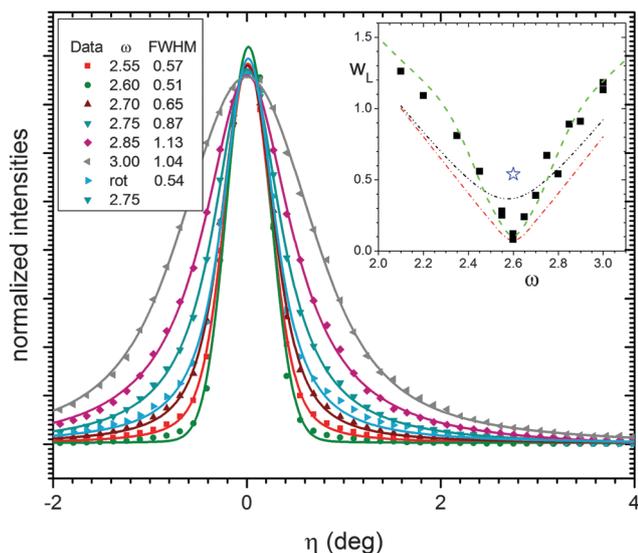
Fig. 5 The symbols show the ring intensity $I_r(\eta)$, normalized to $\eta = 0$ to emphasize increased widths when substrate angle ω was not the Bragg angle θ_B. The ring data are from the same exposures of DMPC that produced the rocking scans in Fig. 3a. The lines show the Voigtian fits that have Lorentzian FWHM w_L shown in the inset. The inset also includes w_L for all the exposures in Fig. 3a. The lower red dashed-dot line in the inset uses eqn (2) with the constraint $w_L = 0.06°$. The dashed-dot-dot line is an unconstrained fit to eqn (2). The green dashed line is from Fig. 6. The star symbol shows w_L obtained from an exposure that employed continuous rotation over ω.

a less well ordered fraction $f_2 = 1 - f_1$ with $w_{M2} = 1.0°$, so the total intensity would be

$$I_r(\eta,\omega) = f_1 I_r(\eta,\omega,w_{M1}) + (1 - f_1)I_r(\eta,\omega,w_{M2}). \quad (3)$$

The shape of $w(\omega)$ for the case $f_1 = 0.5$ in Fig. 6 is qualitatively similar to the shape of $w_L(\omega)$, as shown in the inset to Fig. 5,
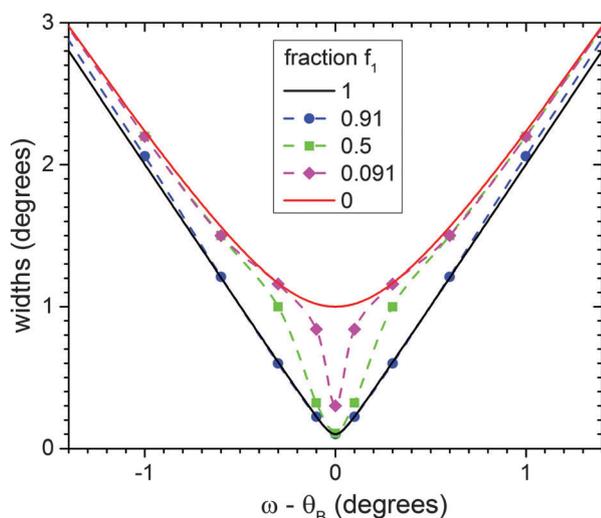

Fig. 6 The widths (FWHM) of the sum of two Lorentzians in eqn (3). The fraction of the total intensity in the first Lorentzian is f_1. The first Lorentzian was given width $w_{M1} = 0.1°$ and the second Lorentzian was given width $w_{M2} = 1.0°$.

suggesting that we may gain insight from this toy model. We first note that, for all cases, $w(\omega)$ behaves asymptotically as $2|\omega - \theta_B|$ for large enough ω and is quadratic in $|\omega - \theta_B|$ for the smallest ω. For the pure models $f_1 = 0$ and 1, there is a smooth transition between these asymptotic limits with monotonically increasing magnitude of the slope with increasing $|\omega - \theta_B|$. However, for mixed models, instead of a monotonic increase, the slope of $w(\omega)$ exceeds 2 for intermediate angles. Understanding the reason for this behavior is important. When $\omega = \theta_B$, the intensity $I_{r1}(\eta)$ from the narrow Lorentzian dominates the sum even when f_1 is as small as 0.091, as shown in Fig. 6, so $w(0)$ is closer to w_{M1} than to w_{M2}. In contrast, as ω increases, the $(\omega - \theta_B)^2$ term in eqn (1) dominates the w_{M1}^2 term in I_{r1} but not the w_{M2}^2 in I_{r2}, so for small enough f_1, $w(\omega)$ is closer to w_{M2} than to w_{M1}. Unfortunately, this means that the mosaicity obtained from the classic rocking scans or from the equivalent fixed angle ring plots at the Bragg angle $\omega = \theta_B$ focuses mainly on the best ordered part of a sample and, if there are more disordered parts, this under reports their presence. Such under reporting is diagnosed by $w_L(\omega)$ plots.

5. Results for additional samples

Thus far, we have presented results mainly for our best studied dry DMPC sample. We find that other samples have qualitatively similar rocking $I_R(\omega)$ that are reasonably well fit with Lorentzians and ring $I_r(\eta)$ intensities that are reasonably well fit with Voigtians. According to the insight gained from the previous section, we here focus on the $w_L(\omega)$ results obtained from the ring intensities for sequences of fixed angles ω.

Of course, the toy model should not be taken to infer that deviations from eqn (2) mean that there are simply two Lorentzian distributions. Rather, such deviations imply that the distribution is more complex than a single Lorentzian. Nevertheless, it will be convenient to write that such deviations are evidence for a heterogeneous mosaic distribution and to quote the smallest value of w that corresponds to both the rocking scan and to the Bragg angle ring data alongside an average w_M that is obtained by fitting eqn (2) to all the $w_L(\omega)$ results, as shown by the dashed-dot-dot line in the inset to Fig. 5.

Mosaic spread varies from sample to sample, even for the same lipid, depending upon particulars of the deposition, and it even varies in the same sample at different locations on the Si wafer. Fig. 7a shows results for a poorly oriented sample of DMPC with minimal $w_L \approx 3°$. This shows that results from two different orders agree and that eqn (2) works quite well. However, the smallest w_L is 2.9° compared to 3.1° for the fit of eqn (2) to all w_L, consistent with a small amount of heterogeneity. Results for another DMPC sample are shown in Fig. 7b. As in Fig. 7a, the mosaic results for different orders agree well. This figure shows the advantage of having higher orders because the range of $\omega - \theta_B$ is greater since our non-transparent substrate blocks the beam when $\omega < 0$ and it blocks the diffraction peak for $\omega > 2\theta_B$. (Essentially transparent substrates are available for neutron studies that allow angles
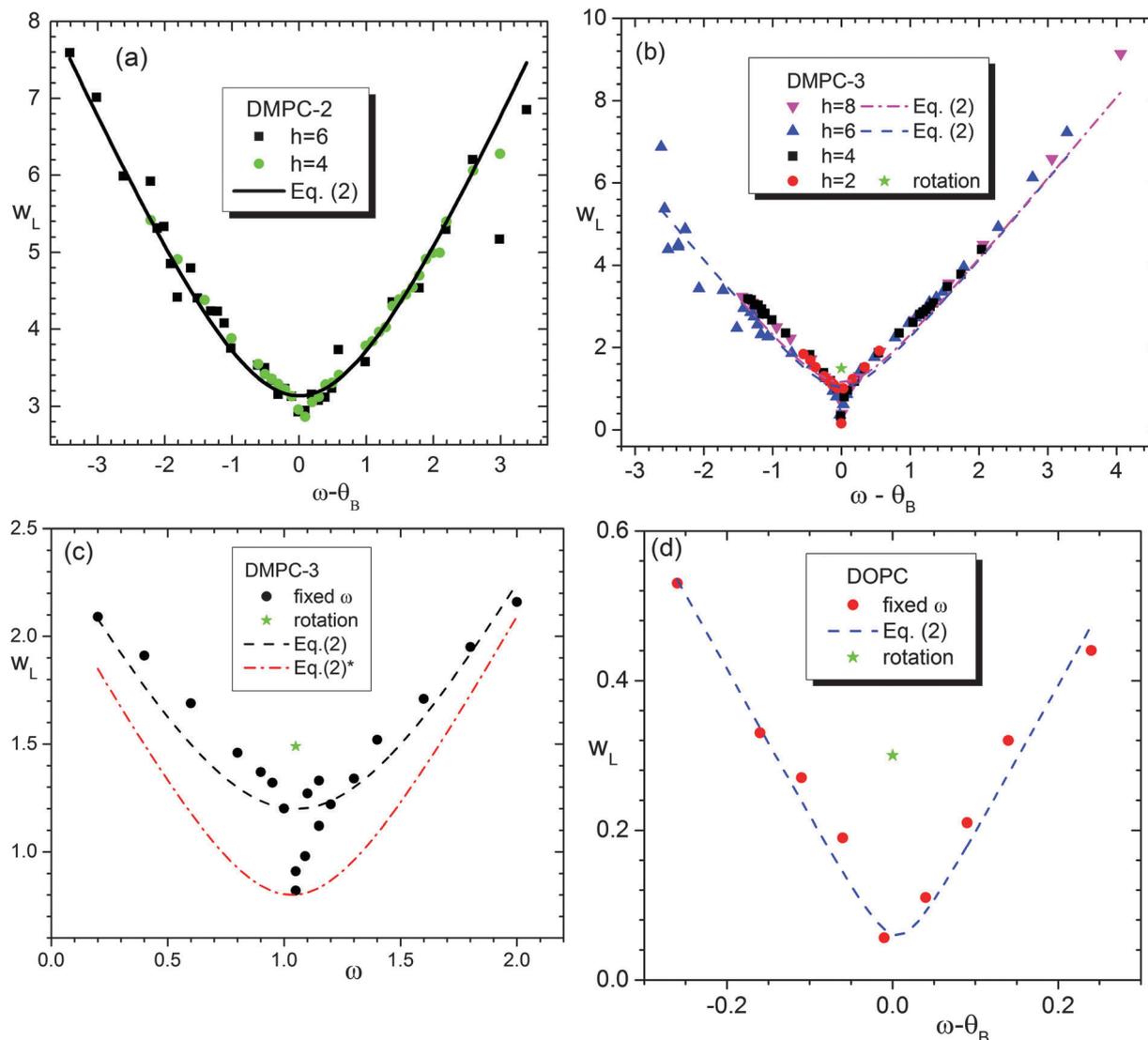
Fig. 7 Lorentzian widths w_L obtained from Voigtian fits of the ring intensities $I_r(\eta)$ as a function of the difference in the substrate angle ω and the Bragg angle θ_B of diffraction peaks. All angles are in degrees. The lines show fits to eqn (2). (a) Poorly oriented dry DMPC for orders $h = 4$ and $h = 6$ with $D = 53.5$ Å. (b) Even orders of moderately well oriented dry DMPC with $D = 54.7$ Å. (c) Same DMPC sample as in (b), but hydrated with $D = 63.8$ Å and $h = 2$ only. The dot-dash line fit had w_L constrained to its minimal value. (d) Hydrated DOPC with $D = 60.4$ Å, $h = 2$. The stars in (b–d) show w_L for continuously rotated exposures.

outside this range, although there is significant absorption by the sample itself for ω near 0 and $2\theta_B$.[23,24]) This sample is better ordered than the one in Fig. 7a, with $w_M = 1.1°$ for the overall fit. It is not as well oriented as the one in Fig. 5 where the inset shows that the overall fit to the data using eqn (2) is $w_M \approx 0.4°$. The shape of the curve in Fig. 7b for small $\omega - \theta_B$ clearly indicates heterogeneity in the sample with $w_L \approx 0.1°$ for the rocking scan and for the $\omega = \theta_B$ ring. Shortly after taking those data the sample was hydrated with the result shown in Fig. 7c. As the higher orders are not visible in hydrated samples, and as the beam size dominates the $h = 1$ ring data, $h = 2$ was best for analysis. Compared to the dry sample, the width from the rocking scan and the $\omega = \theta_B$ ring increased to about $0.8°$ while the fit to all the data only increased from $1.1°$ to $1.2°$.

In our hands, the lipid DOPC has the smallest mosaic spread. Fig. 7d shows the $w_L(\omega)$ plot for the $h = 2$ peak of a well hydrated DOPC sample. The shape of the graph is consistent with a single Lorentzian mosaicity. Even though the beam width was reduced to effectively $0.2°$ by increasing the sample to detector distance, w_L for the smallest $\omega - \theta_B$ has a large fractional uncertainty, but it is nevertheless clear that the true mosaic width is $0.05°$ or less.

6. Additional considerations

The finite size L_r of domains in the in-plane radial direction provides a lower bound on the mosaic width w that can be obtained from ring data. This is because the Bragg peaks that

would occur with no mosaicity and infinite L_r become Bragg sheets for finite L_r which have off specular intensity proportional to $\mathrm{sinc}^2(q_r L_r/2)$ at $q_z = 2\pi/D$ with FWHM $\approx \sin^{-1}(0.89\lambda/L_r)$ given by the Scherrer formula.[25] For small w and short exposures used for rocking scans, the rings are measurable only for small values of η and then they can not be separated experimentally from a Bragg sheet unless an impractically large sample to detector distance is employed. For $L_r = 1000$ Å, which is the small end of our estimated range for L_r, this gives a measurable lower bound of $0.06°$. This should be considered for the DOPC sample in Fig. 7d for which we did not take long exposures with the finger attenuator; Fig. 7d would therefore be consistent with an even smaller mosaic spread than the minimal value indicated in the inset. We also note that the maximal oscillations in the $\mathrm{sinc}^2(q_r L_r/2)$ function also decay only as $1/q_r^2$ which becomes essentially a Lorentzian decay when a distribution of domain sizes L_r is considered.

There are two complications for measuring mosaic spread in well hydrated stacks of fluid phase L_α lipid bilayers. The first complication is that the higher order peaks become weak and even disappear. This is the well known phenomenon that smectic liquid-crystalline disorder drains intensity away from the lamellar peaks into power law tails and diffuse scattering.[26] This means that mosaic spread has to be determined on lower order peaks. For the same sample to detector S distance, the angular resolution is reduced for the ring method, namely, the angle subtended by the beam width is larger. Fortunately, this can be compensated by making S larger, and this is what was done for the DOPC sample in Fig. 7d and the DMPC sample in Fig. 7c.

The second complication for well hydrated samples is the diffuse scattering. Instead of the delta function Bragg peak at $q = q_B$ for an ideal crystal, the structure factor decays gradually as q deviates from q_B. However, for the ideal case when there is no mosaicity, theoretical calculation exhibits no sharp rings in this diffuse scattering. One may therefore subtract the broad diffuse scattering from the ring scattering to obtain the intensity that identifies the mosaic distribution.

7. Discussion and conclusions

Our initial concern that rocking curves and rings appeared to give different values of mosaic spread has been resolved. Unsurprisingly, as they are simply orthogonal views of the overall mosaicity and the samples are in-plane isotropic, we find that the rocking scan and the Bragg peak ring give the same value for the mosaic spread. Both methods indicate that the mosaic distribution has long tails, more consistent with a Lorentzian than a Gaussian, although the ring method indicates a tail that is somewhat shorter than a Lorentzian for our most extensively analyzed dry sample. As recent papers that determine pole figures emphasize,[11–13] such determinations are greatly facilitated by the use of area detectors. Compared to the traditional rocking scan, an advantage of analyzing a Bragg ring is that fewer exposures are required and the angular range is not limited (due to a non-transparent substrate) to the $[0,2\theta_B]$ range of rocking scans. A disadvantage of using Bragg rings is that the mosaic distribution must be deconvoluted from the beam shape, but that can be alleviated by choosing a large sample to detector distance.

Rocking and Bragg ring data yield quite small values for the mosaic spread in our best samples. This is not, however, the whole story. Our analysis of the rings when the incident angle ω is not the Bragg angle θ_B leads us to conclude that, for the samples in Fig. 7a–c, there is a population of domains that has a larger mosaic spread than what is inferred from the rocking and Bragg ring data because those data are dominated by the best oriented portion of the sample. This also partly helps to account for the appearance of orders on the area detector when the incident angle ω is not the Bragg angle θ_B. The long, roughly Lorentzian, tails also partly account for the appearance of such orders. Furthermore, both these cause the appearance of stronger mosaic rings when the sample is rotated continuously as used in our LAXS protocol. However, for DOPC the mosaic spread appears to be a single Lorentzian distribution with very small mosaic spread as shown in Fig. 7d. Even DOPC samples sometimes exhibit strong mosaic rings upon rotation,[14] but other more recent samples of DOPC exhibit very weak or even indiscernible mosaic rings when hydrated. Assuming that hydration generally anneals a sample and does not increase its mosaic spread, a reasonable protocol is to take mosaic data on a high order in a dry sample such as shown in Fig. 1. An easier alternative is to analyze the Bragg rings of a rotated sample, which at least appear to provide upper bounds for the mosaic spread as indicated by the stars in the insets to Fig. 5 and 7b–d. Such determinations of mosaic spread may then be used to correct the values of other membrane properties obtained from oriented samples.

Acknowledgements

References

1 Y. L. Wu, K. He, S. J. Ludtke and H. W. Huang, *Biophys. J.*, 1995, **68**, 2361–2369.
2 C. Li and T. Salditt, *Biophys. J.*, 2006, **91**, 3285–3300.
3 D. Krepkiy, M. Mihailescu, J. A. Freites, E. V. Schow, D. L. Worcester, K. Gawrisch, D. J. Tobias, S. H. White and K. J. Swartz, *Nature*, 2009, **462**, 473–479.

4 J. J. Pan, S. Tristram-Nagle and J. F. Nagle, *J. Membr. Biol.*, 2009, **231**, 11–27.

5 T. J. McIntosh and S. A. Simon, *Annu. Rev. Biophys. Biomol. Struct.*, 2006, **35**, 177–198.

6 M. Gandhavadi, D. Allende, A. Vidal, S. A. Simon and T. J. McIntosh, *Biophys. J.*, 2002, **82**, 1469–1482.

7 J. Mattai, P. K. Sripada and G. G. Shipley, *Biochemistry*, 1987, **26**, 3287–3297.

8 W. J. Sun, R. M. Suter, M. A. Knewtson, C. R. Worthington, S. Tristram-Nagle, R. Zhang and J. F. Nagle, *Phys. Rev. E: Stat. Phys., Plasmas, Fluids, Relat. Interdiscip. Top.*, 1994, **49**, 4665–4676.

9 R. P. Rand and V. A. Parsegian, *Biochim. Biophys. Acta*, 1989, **988**, 351–376.

10 Y. F. Liu and J. F. Nagle, *Phys. Rev. E: Stat., Nonlinear, Soft Matter Phys.*, 2004, **69**, 040901.

11 S. Gaudet, K. De Keyser, S. Lambert-Milot, J. Jordan-Sweet, C. Detavernier, C. Lavoie and P. Desjardins, *J. Vac. Sci. Technol., A*, 2013, **31**, 021505.

12 J. L. Baker, L. H. Jimison, S. Mannsfeld, S. Volkman, S. Yin, V. Subramanian, A. Salleo, A. P. Alivisatos and M. F. Toney, *Langmuir*, 2010, **26**, 9146–9151.

13 C. Mocuta, M. I. Richard, J. Fouet, S. Stanescu, A. Barbier, C. Guichet, O. Thomas, S. Hustache, A. V. Zozulya and D. Thiaudiere, *J. Appl. Crystallogr.*, 2013, **46**, 1842–1853.

14 Y. Lyatskaya, Y. F. Liu, S. Tristram-Nagle, J. Katsaras and J. F. Nagle, *Phys. Rev. E: Stat., Nonlinear, Soft Matter Phys.*, 2001, **63**, 011907.

15 T. Salditt, C. Li, A. Spaar and U. Mennicke, *Eur. Phys. J. E: Soft Matter Biol. Phys.*, 2002, **7**, 105–116.

16 N. Chu, N. Kucerka, Y. F. Liu, S. Tristram-Nagle and J. F. Nagle, *Phys. Rev. E: Stat., Nonlinear, Soft Matter Phys.*, 2005, **71**, 041904.

17 T. T. Mills, G. E. S. Toombes, S. Tristram-Nagle, D. M. Smilgies, G. W. Feigenson and J. F. Nagle, *Biophys. J.*, 2008, **95**, 669–681.

18 A. L. Boscia, K. Akabori, Z. Benamram, J. A. Michel, M. S. Jablin, J. D. Steckbeck, R. C. Montelaro, J. F. Nagle and S. Tristram-Nagle, *Biophys. J.*, 2013, **105**, 657–666.

19 M. Vogel, C. Munster, W. Fenzl, D. Thiaudiere and T. Salditt, *Phys. B*, 2000, **283**, 32–36.

20 S. Tristram-Nagle, R. Zhang, R. M. Suter, C. R. Worthington, W. J. Sun and J. F. Nagle, *Biophys. J.*, 1993, **64**, 1097–1109.

21 S. A. Tristram-Nagle, *Methods Mol. Biol.*, 2007, **400**, 63–75.

22 S. L. Barna, M. W. Tate, S. M. Gruner and E. F. Eikenberry, *Rev. Sci. Instrum.*, 1999, **70**, 2927–2934.

23 N. Kucerka, D. Marquardt, T. A. Harroun, M. P. Nieh, S. R. Wassall, D. H. de Jong, L. V. Schafer, S. J. Marrink and J. Katsaras, *Biochemistry*, 2010, **49**, 7485–7493.

24 N. Kucerka, M. P. Nieh, J. Pencer, J. N. Sachs and J. Katsaras, *Gen. Physiol. Biophys.*, 2009, **28**, 117–125.

25 A. Guinier, *X-Ray Diffraction in Crystals, Imperfect Crystals and Amorphous Bodies*, W. H. Freeman and Company, San Francisco, 2nd edn, 1963.

26 J. F. Nagle, R. T. Zhang, S. TristramNagle, W. J. Sun, H. I. Petrache and R. M. Suter, *Biophys. J.*, 1996, **70**, 1419–1431.